Green Chemistry

Accepted Manuscript

ROYAL SOCIETY OF CHEMISTRY

www.rsc.org/greenchem

Synthesis of glucose-mediated Ag - γ-Fe_2O_3 multifunctional nanocomposites in aqueous medium - a kinetic analysis of their catalytic activity for 4-nitrophenol reduction

Received 00th January 20xx,
Accepted 00th January 20xx

DOI: 10.1039/x0xx00000x

www.rsc.org/

Mandeep Kaloti,[a,b] Anil Kumar[* a,b] and Naveen K. Navani [a,c]

This paper reports the synthesis of γ-Fe_2O_3 supported Ag nanoparticles (NPs) in aqueous medium by following the green approach. The presence of Fe_2O_3 in gamma phase and silver in the nanocomposite has been confirmed by Raman spectroscopy, EDAX and XPS analyses. The presence of Ag in the nanocomposite is also indicated by UV spectroscopy. In the process of *in situ* generation of glucose mediated Ag NPs on γ-Fe_2O_3 matrix reduced the size of γ-Fe_2O_3 nanoclusters from 11.6 ± 1.6 to 9 ± 1 nm as was estimated from HRTEM analysis. Glucose served as an effective stabilizer for both Ag and γ-Fe_2O_3 in the nanocomposite. At lower concentrations of Ag (0.15 - 1.2 μM) the reduction of the 4-nitrophenol (4-Nip) follows pseudo-first-order kinetics and the second order rate constant for this process was found to be 5.28×10^3 dm^3 mol^{-1} s^{-1}. Whereas, at higher concentrations (3.2 - 28.9 μM), it follows zero-order kinetics and occurred with a rate constant of 1×10^{-2} mol dm^{-3} s^{-1}. The amount of silver in the nanocomposite is found to influence the kinetics of the catalytic reduction in a complex scheme following the Langmuir-Hinshelwood mechanism. The recyclability of the as synthesized nanocomposite up to 7 cycles and the catalytic effect even at very low silver (0.15 μM) associated with high surface area and superparamagnetism suggests it to be the cost effective and environmental friendly potential catalytic system.

Introduction

During the last few decades, magnetic nanoparticles (MNPs) have attracted wide attention due to its unique properties such as superparamagnetism, low Curie temperature, high coercivity, high magnetic susceptibility and high surface area.[1] These features render them the great potential for various applications like magnetic storage devices,[2] ferrofluids,[3] magnetic separation/biomolecular purification,[4] MRI contrast agents, targeted drug delivery,[5] hyperthermia,[6] immunoassay,[7] biosensing,[8] tissue regeneration,[9] cell sorting,[10] molecular interaction in live cells[11] and catalysis.[12] For most of the biomedical applications, it is desirable to make them water soluble containing biocompatible components.

For achieving these features, MNPs have generally been coated by a variety of organics and inorganics. Organics generally included the natural (glucose/dextran,[13] chitosan,[14] alginate[15] and starch[16]) and synthetic (poly(vinyl alcohol) (PVA)[17], poly(ethyleneglycol) (PEG)[18], poly(vinylpyrrolidone) (PVP)[19], poly(acrylic acid) (PAA)[20], Poly(N-isopropylacrylamide) (PolyNIPAAM)[21], poly(lactic-co-glycolic acid) (PLGA)[22], poly(methylacrylic acid) (PMAA)[23] and polyethyleneimine[24]) polymers. Inorganic materials such as quantum dots,[10] gold,[25] porous silicon[26], silica,[27,28] silver[28] and graphene oxide[29] have been extensively used for coating of MNPs.

Metal nanoparticles (NPs) are finding increasing applications in energy conversion, petrochemical industries and oil refineries as they catalyze various conversions like C-C cross coupling, hydrogenation-dehydrogenation, electron transfer reaction and hydrocarbon oxidation.[30] The repetitive use of the catalyst, however, requires the metal NPs to be loaded onto a supporting material having nano/microstructures so as to produce an effective heterogeneous catalyst. Recently, the use of iron oxide (Fe_3O_4) NPs as supporting material has drawn a great deal of attention because of their biocompatibility, reusability and economic viability. Moreover, these particles exhibit high magnetization, which makes them suitable for biomedical as well as catalytic applications allowing their easy separation using a magnet. In this context, the functionalization of the MNPs with Ag NPs to form binary hybrids has been widely studied in order to investigate their applications in negative magnetoresistance,[31] in catalysis for performing epoxidation of styrene[32] and 4-nitrophenol reduction[33] and for biological applications like antimicrobial activity[34] and drug release.[35] Compared to Pt,[33] Pd,[36] Ru[37] and Au[33,38-39], silver[39-43] is relatively inexpensive and possesses good physical and chemical properties including the catalytic as well as antimicrobial activity. In these studies the catalytic reduction of 4-nitrophenol (4-Nip) to 4-aminophenol (4-Ap) has been considered as a standard benchmark reaction for easy assessment of catalytic activity of metal NPs in aqueous medium.[33-43] Previous studies on such systems have employed magnetite NPs as a matrix/support to the Ag NPs.[28,41-44] However, the use of magnetite poses several challenges as it is unstable in air and tends to undergo phase transformation to yield Fe_2O_3 with a reduction in magnetization and loss of dispersibility.[1,45] The development of an efficient, workable

[a] *Centre of Nanotechnology, Indian Institute of Technology Roorkee, Roorkee-247667, India.*
[b] *Department of Chemistry, Indian Institute of Technology Roorkee, Roorkee-247667, India. *E-mail: anilkfcy@iitr.ac.in*
[c] *Department of Biotechnology, Indian Institute of Technology Roorkee, Roorkee-247667, India.*

Electronic Supplementary Information (ESI) available: [optical spectra, FTIR, FESEM images and their elemental mapping, kinetic control experiments, kinetic trace for the reduction of 4-Nip at an intermediate concentration of 2.4 μM Ag exhibiting transition between first- and zero-order kinetics and depicting the role of glucose as reducing agent as compared to $NaBH_4$.See DOI: 10.1039/b000000x

catalyst requires having the support material to be fairly stable in natural environment with relatively high magnetization (without any change in phase) for easy separation, coated with inexpensive metal catalyst at very low concentration. In the literature we have came across a report employing commercial γ-Fe_2O_3 NPs loaded with a relatively much higher amount of Ag NPs (52 wt %).[45]

The present MS for the first time has reported the synthesis of glucose-mediated Ag- γ-Fe_2O_3 nanocomposites with a specific objective of using γ-Fe_2O_3 as a support material owing to its relatively higher magnetization and biocompatibility in aqueous medium. The *in situ* generation of Ag NPs at its lower concentration (0.6 – 3.2 μM) by the reduction of Ag^+ using glucose as a stabilizer as well as reducing agent in the presence of γ-Fe_2O_3 results in the production of fairly smaller γ-Fe_2O_3 nanoclusters. These nanocomposites have been characterized in terms of their size, optical, magnetic and catalytic properties.

The present work makes use of non-toxic precursors and aqueous medium to design a catalytic system consisting of biocompatible magnetic nanoparticles support loaded with non-toxic catalyst (Ag) at its low concentrations. This catalyst has been successfully utilized for the conversion of hazardous material like 4-Nip to useful environmental benign product, 4-Ap and demonstrates several advantages over the existing catalytic systems in terms of being efficient, recyclable and magnetically separable, requiring very small amount of the catalyst besides being environmentally benign. All these features suggest it to be environmental friendly green material for performing sustainable catalytic processes. The preliminary biological experiments designed with this nanocomposite have demonstrated its efficient antimicrobial activity.

Experimental section

Reagents

Ferric sulphate hydrate (Thomas Baker), ferrous sulphate heptahydrate, silver nitrate and glucose (BDH), 4-nitrophenol (99 %) (SISCO research lab Pvt. Ltd), ammonium hydroxide (25%) and sodium borohydride (Merck). All chemicals used were of analytical grade. All water used in the experiments was of Millipore grade deionized water (DIW).

Equipment

The electronic spectra and the kinetic studies were recorded on a Shimadzu UV-VIS 1601S spectrophotometer equipped with temperature controller. The X-ray diffraction patterns of powder samples were recorded on a Bruker AXS D8 Advance X-ray diffractometer using Cu Kα radiation (1.5418 Å) as the X-ray source. The morphology and elemental analysis of the nanocomposites were studied on a field emission scanning electron microscope (FESEM, FEI-QUANTA 200-FEG) equipped with an energy dispersion X-ray spectrometer using an accelerating voltage of 20 kV. The surface morphology of the nanostructures was analyzed recording their 2D and 3D images on an atomic force microscope (AFM) supplied by Molecular Tools and Devices for Nanotechnology equipped with NOVA software using semi-contact mode. Electron micrographs and selected area electron diffraction (SAED) patterns were recorded on a transmission electron microscope (FEI-TECNAI G2 20 S-TWIN) at an accelerating voltage of 200 kV. The zeta potential of nanocomposites was recorded on a Malvern Zetasizer ZS90 equipped with 632 nm He–Ne laser. Infrared (IR) spectra were recorded in the mid IR range (4000 - 400 cm^{-1}) in KBr medium on a Thermo Nicolet Nexus Fourier transform infrared (FTIR) spectrometer. Raman measurements were made on an inVia Renishaw spectrophotometer equipped with Ar ion 514 nm laser having a resolution of ± 1 cm^{-1} and a 2.5 μm confocal resolution. Surface area of the samples was analyzed using five point Brunauer–Emmett–Teller (BET) method on a NOVA 2200e High Speed Automated Surface Area Analyzer. The X-ray photoelectron spectroscopy was performed on a PHI 5000 Versa Probe II supplied by ULVAC-PHI Inc., Japan equipped with monochromatic Al K_α 945 radiation source. Magnetic measurements of the samples were carried out on Vibrating Sample Magnetometer (VSM) using PAR 155 and MCFMS-3 cryogenic free miniVSM system with pulse cryocooler at 300 K.

Methodology

Synthesis of γ-Fe_2O_3 NPs and silver coated γ-Fe_2O_3 (Ag – γ-Fe_2O_3) nanocomposites

The γ-Fe_2O_3 NPs (SB) were prepared by using an earlier reported method[46] with a slight modification and is described briefly. Ferrous sulphate (0.75 g) and ferric sulphate (0.46 g) were dissolved in 100 mL DIW at 40^0 C and the pH of the solution was maintained at 3 using ammonium hydroxide (25%) and stirred for 30 min in order to precipitate the iron hydroxides. The pH of this solution was further increased by adding ammonium hydroxide solution under stirring to 10.5. After about 30 min it resulted in the formation of blackish brown NPs. These particles could be separated magnetically and washed with DIW several times till the pH is around 9.5. The particles, thus produced were found to be negatively charged using zeta probe of about -27mV.

To the above synthesized γ-Fe_2O_3 NPs (SB), silver nitrate of varied concentrations (0.15 - 28.9 μM) were added slowly. This reaction mixture was stirred for about 15 min followed by sonication for another 10 min. Thereafter, glucose solution, having about 5 times higher concentration to that of silver nitrate, was added drop-wise and stirred further for 30 min at 50^0 C. This excess amount of the glucose was added to ensure the complete reduction of Ag NPs. The Ag coated particles were then washed with DIW in order to remove any free/unbound Ag NPs. The resulting Ag – γ-Fe_2O_3 nanocomposites were subjected to further characterization. In a control experiment, Ag NPs were also generated in the absence of matrix using the same concentration of Ag^+ and glucose (Fig. S1, ESI†). These NPs have absorption maximum at around 396 nm.

Powder samples were obtained by drying the sample in a vacuum oven at 50 °C for 3 h, which were used for the analysis of XRD, BET, FTIR analyses and Raman spectroscopy.

Preparation of samples for various analyses

For recording the electronic spectra diluted solution of the Ag – γ-Fe_2O_3 samples were used. For Raman analysis, the instrument was calibrated using silicon reference at 520 cm^{-1} prior to use. The powder sample was placed on the glass substrate and the measurements were carried out using 514 nm argon ion laser in the wavenumber range of 200 - 1200 cm^{-1}. All measurements were made at low laser power of 0.5 mW to avoid any kind of damage to the samples. For AFM and FESEM analyses, the diluted samples were applied on the glass substrate, which was dried at 40 °C in vacuum oven. For FESEM analysis, the prepared sample were further coated with gold in order to make them conducting. For TEM analysis, a small diluted sample drop was applied to a 200 mesh carbon coated copper grid and dried at room temperature. Powdered samples were used for characterization of FTIR, BET and XPS. For magnetic measurements, a known amount of the powdered samples taken in a polymer capsule were used.

Kinetic conditions for catalytic reduction of 4-Nip

Catalytic activity of silver coated γ-Fe_2O_3 nanocomposites was examined by performing the kinetics of the model reaction, involving the reduction of 4-Nip at its surface using $NaBH_4$ as reducing agent. In these experiments, the concentration of $NaBH_4$ (51.1 - 119.3 mM), γ-Fe_2O_3 NPs (28.77 mM) and 4-Nip (62.5 - 193.5 µM) were kept such that these were more than ten times higher to those of the concentration of Ag NPs in order to maintain the pseudo-kinetic conditions. The thermodynamic parameters were evaluated by performing the kinetics in the temperature range of 293K to 323K.

The catalytic activity of the synthesized Ag – γ-Fe_2O_3 nanocomposites were analyzed spectrophotometrically by performing the reduction of 4-Nip to 4-Ap. All the kinetic experiments were performed in 1 cm quartz cuvette. In these reactions, 0.1mL of 4-Nip solution of varied concentrations (2 - 5.5 mM) was added into 1.98 mL DIW followed by the addition of freshly prepared 1 mL of 0.2 mol dm^{-3} $NaBH_4$. To this reaction mixture, 20 µL of the varied amount of Ag on γ-Fe_2O_3 (28.77 mM) was added to keep the total volume at 3.1 mL. After the addition of the catalyst, the time immediately after the induction period was considered as to be t = 0 denoted as t_0. The progress of the reaction was then monitored by following the decrease in absorbance due to consumption of 4-Nip at 400 nm.

The reusability of the above synthesized nanocatalyst(s) was also examined by repetitive use of the same catalyst for performing the above reaction. In these experiments, the nanocomposite used to catalyze the reaction was separated magnetically, washed with distilled water and reused seven times for performing the reaction.

Results and discussion

Optical spectra

The γ- Fe_2O_3 NPs (SB) used as matrix exhibits a broad absorption peak at 425 nm and a shoulder at 485 nm. The addition of Ag^+ to the γ-Fe_2O_3 matrix results in the increase in its absorbance associated with a slight red shift in absorption peaks to 430 and 495 nm respectively. At low [Ag^+] (0.6 µM), its *in situ* reduction by glucose results in a blue shifted absorption spectrum exhibiting a broad peak at 395 nm and a shoulder at 499 nm. The drastic change in absorbance upon the reduction of Ag^+ is understood by the formation of Ag NPs on the surface of the matrix, and the resulting nanocomposite is termed as SPLAg. Moreover, at a higher concentration of silver (6.4 µM), it exhibited a further blue shifted spectrum with both peaks shifted to the blue region and this nanosystem is denoted by SPHAg. The blue shifted spectrum at a higher concentration of silver might have arisen due to further reduction in the size of the Ag – γ- Fe_2O_3 NPs. It is likely that the γ- Fe_2O_3 NPs are also becoming smaller in the presence of Ag NPs, which was reflected by their increased dispersity. This aspect was further examined, by plotting the additive spectra consisting of matrix and Ag NPs, prepared in the absence of matrix, at its two used concentrations (Fig. S1 curves b and c, ESI^+). A comparison of the additive spectra with those obtained

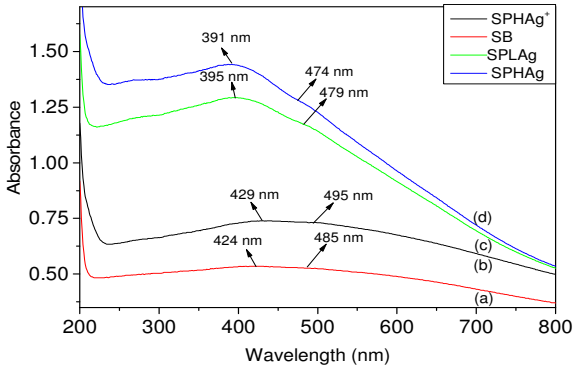

Fig. 1 UV-visible spectra of the SB (a) (supporting matrix) and the matrix coated by typical low (c) (SPLAg) and high (d) (SPHAg) concentrations of Ag NPs generated in *in situ* reaction.

by the *in situ* generation of Ag NPs (Fig. S1 d and e, ESI^+) clearly shows the latter to be more intense and fairly broad. It suggests some changes either in their morphology or some type of interaction between the two resulting in the observed change(s).

XRD

Fig. 2 shows the XRD pattern of the as synthesized samples: SB, SPLAg and SPHAg. All the reflections due to SB corresponded to γ-Fe_2O_3 (JCPDS file no. 39-1346) having cubic structure. The addition of low silver in SPLAg results in the development of two new peaks corresponding to (110) and (200) planes due to Ag NPs. In case of SPHAg, apart to the peaks due to γ-Fe_2O_3 Ag NPs in SPLAg an additional reflection

from (220) planes of Ag matching with its cubic structure (JCPDS file no. 001-1167) was also observed. These data clearly support the formation of Ag – γ-Fe_2O_3 nanocomposites. The size of the γ-Fe_2O_3 and Ag NPs in SB, SPLAg and SPHAg were determined using Debye-Scherrer equation. The size of the γ-Fe_2O_3 in these samples was found to be 12 ± 1.1, 11.2 ± 0.9, 8.9 ± 1, respectively. The size of Ag NPs in SPLAg and SPHAg was determined to be 6 ± 0.7 and 6.4 ± 0.4 nm, respectively. A decrease in size of γ-Fe_2O_3 NPs with increasing Ag concentration is in line with that of the observation made by the optical absorption data.

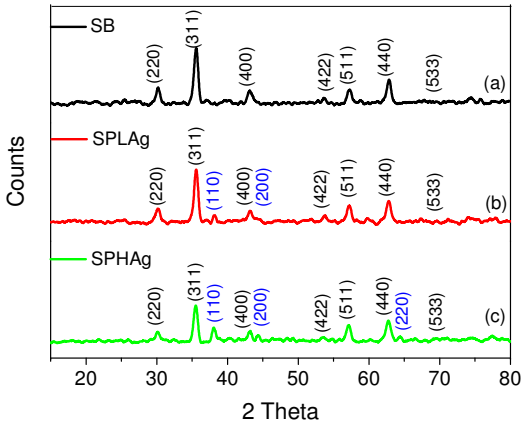

Fig. 2 XRD patterns of SB (a), SPLAg (b) and SPHAg (c).

FTIR and Raman spectra

FTIR spectra of pure SB and SPHAg are presented in Fig. S2, ESI† and the corresponding spectral data is summarized in Table S1, ESI†. The IR spectrum of SB exhibits characteristic peaks due to maghemite phase at 630, 571 and 436 cm^{-1}.[48] FTIR spectra of SPHAg exhibits various prominent bands (cm^{-1}) at: 437, 567, 630, 808, 973, 1113, 1317, 1400, 1620, 2887, 2924, 3225 and 3433. Peaks at 630, 567 and 437 cm^{-1} indicate the presence of γ-Fe_2O_3 in this sample (Fig. 3A), which are different to those of the peaks reported for Fe_3O_4[47] in this region. Other peaks at 1398, 1312, 1116, 1054, 978 and 810 cm^{-1} have been assigned to the asym and sym stretching of SO_4^{2-} in both the cases, which are contributed by the used precursors $FeSO_4$ and $Fe_2(SO_4)_3$.[48] In the case of SPHAg, two additional peaks are observed at 2857 and 2924 cm^{-1}, which matched with the -CH stretching. A broad peak at 3400 cm^{-1} can be assigned to -OH stretching arising due to the adsorbed water on the surface of these particles. Thus, IR spectroscopy clearly indicated the presence of γ-Fe_2O_3 in both the samples. The identification of the iron oxide phase in SPHAg was also probed by recording their Raman spectrum (Fig. 3 b). Its Raman spectrum exhibits the presence of four prominent peaks at about 352, 500, 666 and 718 cm^{-1}, all these peaks matched with those of γ-Fe_2O_3 phase reported in the literature.[47,49,50]

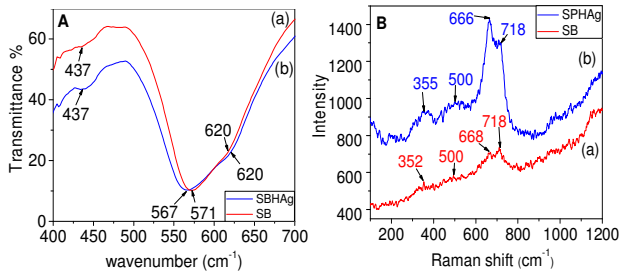

Fig. 3 A FTIR spectra of (a) SB and (b) SPHAg; **B** Raman spectra of (a') SB and (b') SPHAg;

In a control experiment, the Raman spectrum of SB was also recorded. It displayed all the four peaks as observed in SPHAg, thus supporting the presence of γ-Fe_2O_3 in both the samples. Moreover, a comparison of the spectra of SB and SPHAg reveals that the intensity of all the peaks due to vibrational mode of γ-Fe_2O_3 in the latter sample are enhanced by about 3 fold even at low laser power (0.5 mW). This mild increase in the intensity is understood by the SERS effect caused by the presence of Ag in SPHAg involving the chemical enhancement mechanism.[51] It may be pointed out that the Fe_3O_4 phase shows the prominent Raman peaks at 305, 513, 534 and 660 cm^{-1} [50] which are fairly different to those observed in the present system, thereby, rules out the presence of Fe_3O_4 phase in the present system.

XPS

In order to further confirm the phase of iron oxide (Fe_3O_4 or γ- Fe_2O_3) present in the as synthesized sample, surface analysis of 1.2 µM Ag- γ-Fe_2O_3 nanocomposite was performed using XPS analysis (Fig 4). The survey scan spectrum recorded in the range of 0-800 eV exhibits the peaks due to different elements: C, O, Ag and Fe (Fig 4a).The individual narrow scan of each element was subjected to baseline correction and multiple peak fitting for C1s and O1s by using Gaussian software.

The panel (b) exhibits a doublet due to Fe $2p_{3/2}$ and Fe $2p_{1/2}$ at 710.9 and 724.6 eV respectively with a characteristic spin-orbit separation of 13.7 eV,[52] along with a satellite peak at 719.1 eV.[53] The presence of the charge transfer satellite peak indicates that iron is present in the +III oxidation state, differentiating it with
the Fe_3O_4 phase which does not show such a peak due to the presence of iron in a mixed oxidation state of +II and +III.[54] Moreover, the Fe $2p_{3/2}$ peak 710.9 eV and the satellite peak situated around 8 eV higher binding energy to that of Fe $2p_{3/2}$ peak are also characteristics of γ-Fe_2O_3 phase.[55]

Panel (c) exhibits doublet due to Ag $3d_{5/2}$ and Ag $3d_{3/2}$ at binding energies of 366.6 and 372.6 eV, respectively with a spin orbit coupling separation of 6 eV.[56] A shift in the Ag 3d peaks towards lower energy as compare to those of the bulk Ag observed at 368.1 and 374.1 eV[57] indicates the silver in as synthesized nanocomposite to be present in nanodimension.

The high resolution spectrum for C1s region (panel (d)) shows three peaks at binding energies of 283.4, 284.8 and 287.4 eV.

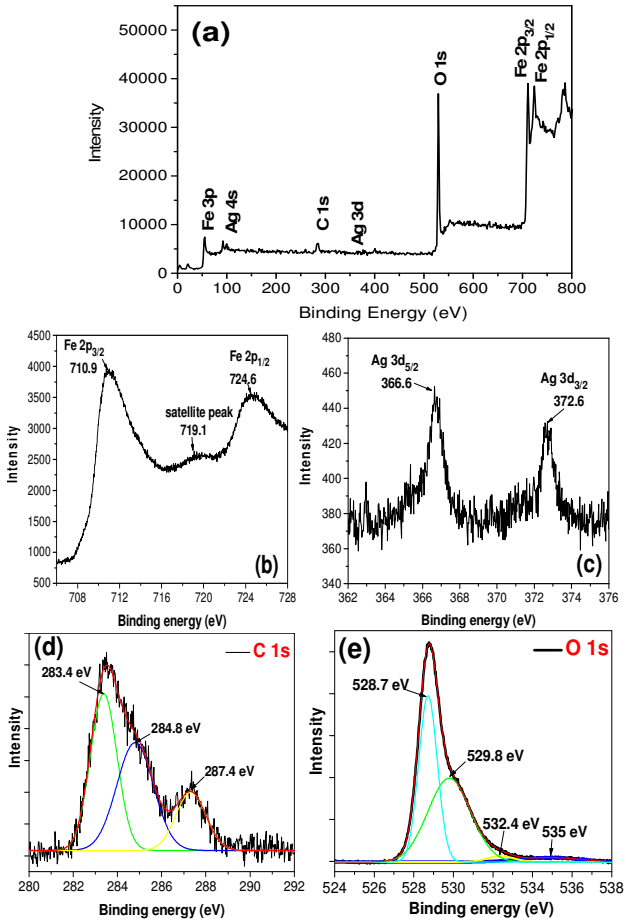

Fig. 4 XPS spectra of SPHAg: Survey scan (a); Narrow scans of the elements: Fe 2p (b); Ag 3d (c); C1s (d) and O 1s (e).

These peaks have been assigned to C-C, C-O and C=O groups respectively.[41] A comparison of these peaks with that of the pure glucose shows them to be shifted at lower energy indicating the glucose moiety to be present in the Ag- γ-Fe_2O_3 composite.[58]

O1s spectrum shows four bands centered at 528.7, 529.8, 532.4 and 535 eV respectively. The intense band at 528.7 eV and a shoulder at 529.8 eV has been assigned to the lattice oxygen and anionic species [59,60] in γ-Fe_2O_3. The bands at higher binding energies 532.4 and 535 eV might have been attributed to the oxygen of glucose and water vapors respectively.[61,62] A slight shift in the binding energy due to glucose functionalities in C1s and O1s region might have arisen because of its weak binding with silver and the matrix in the composite.

XPS analyses of this sample give the atomic % for different elements as: C 1s (14), O 1s (64.1), Fe 2p (21.81) and Ag 3d (0.09), from which the % ratio for Fe/Ag is computed to be 242. Whereas, the calculated atomic % ratio of Fe/Ag, by taking the concentrations of the precursors used for the preparation of γ-Fe_2O_3 and Ag, comes out to 160. It suggested that fairly high amount of Ag (≥ 66 %) is present on the surface of the Ag - γ-Fe_2O_3 nanocomposites.

AFM

Fig. 5 shows the AFM images of SB and SPHAg along with their respective surface roughness and histogram. The AFM image of SB exhibits aggregated chains of clusters of NPs with the average surface roughness (roughness distribution) of 13 nm (9-19 nm).

The coating of silver causes these chains to be broken and shows the particles to be smaller, more organized and isolated as is clearly indicated by their 3D images. The surface roughness of these particles is reduced to 3.7 nm (1.8 -7 nm).

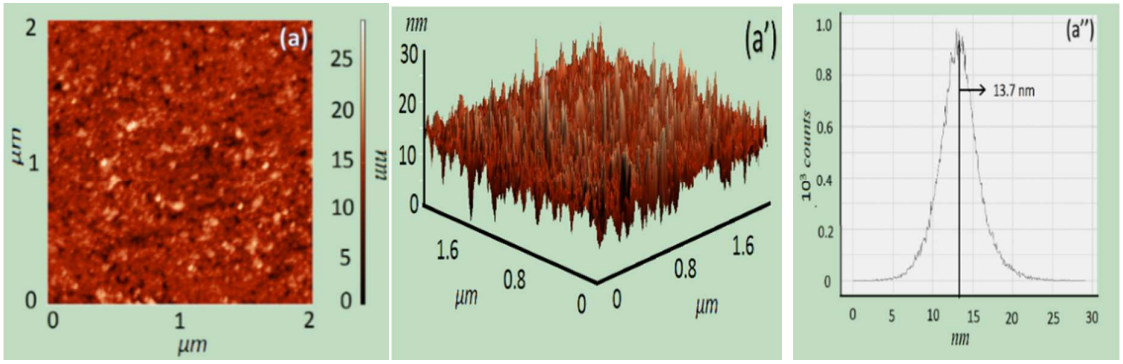

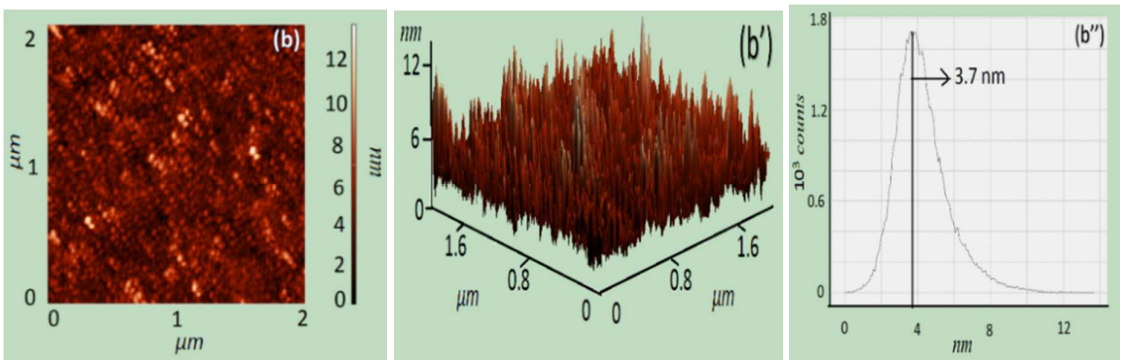

Fig. 5 2D and 3D AFM images of SB (a, b) and SPHAg (a', b'). Surface roughness of the SB and SPHAg is depicted in c and c' respectively.

FESEM

FESEM images of the some representative samples containing pure matrix (SB) and the matrix containing low and high concentrations of Ag NPs along with their EDAX analyses are shown in Fig. 6. The FESEM image of the SB matrix shows it to consist largely the clusters of spherical NPs (Fig. 6 a). Its EDAX analysis shows the presence of Fe and O (Fig. 6 a'). The addition of low amount of silver (SPLAg) causes these particles to assemble resulting in the formation of nanochains in which the size of the particles appears to be slightly reduced (Fig. 6 b). Whereas, at higher Ag concentrations (SPHAg) these nanochains become more compact and the size of the particles in these chains is further reduced (Fig. 6 c). Whereas, EDAX analyses of SPLAg and SPHAg shows the presence of Fe, O, C and Ag in these samples (Fig. 6 b' and c'), in which the atomic weight ratios of Fe and O corresponds to the structure of γ-Fe_2O_3 and the weight percent of silver was low (0.3%) and high (1.04%), respectively. The carbon in these samples is contributed from the reducing agent glucose used for the preparation of Ag NPs. The effect of addition of silver concentration on the morphological changes could be better visualized by FESEM images recorded at lower magnification (Figs. S3 and S4, ESI†). These images clearly show that the large aggregated nanoclusters are broken into smaller units associated with increased organization and a decrease in the size of NPs.

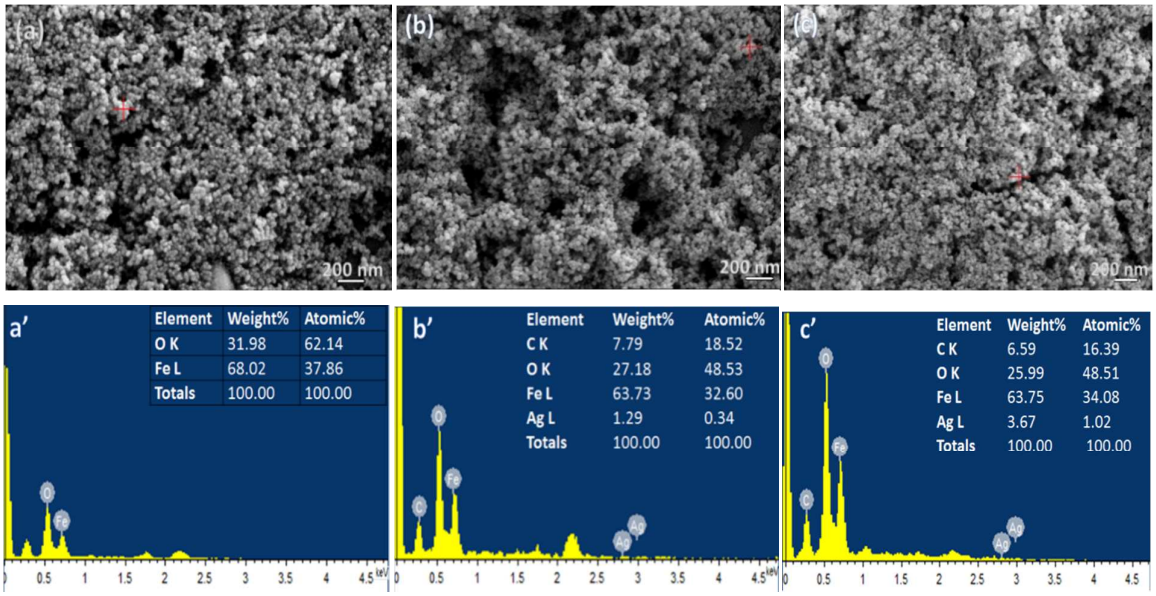

Fig. 6 FESEM images and their respective EDAX analysis on the specific location marked by a cross sign in red of SB (a, a'), SPLAg (b, b') and SPHAg (c, c')

TEM

The morphology and the size/size distribution in these nanostructures were further analyzed by TEM. TEM micrographs, elemental and SAED analyses of these images are presented in Fig. 7. An analysis of these images indicates that the TEM micrograph of SB contains largely clusters of NPs. Whereas, SPHAg seems to have more organized chains of nanoclusters consisting of spherical NPs. EDAX analyses of the

TEM micrographs of SB and SPHAg show the presence of Fe and O in both the samples (Fig. 7 a'' and 7 b''). However, the latter sample also shows the presence of C and Ag.

The SAED analyses of SB and SPHAg exhibit the number of concentric rings containing spots. The indexing of the ring pattern in SB corresponds to the planes (220), (311), (400), (422), (511), (440), (620), (533) and (731) matching with that of γ-Fe_2O_3 phase (JCPDS file No. 39-1346) (Fig. 7 a'''). The indexing of the SAED pattern of SPHAg also exhibits the planes (220), (311), (400), (422), (511), (440) and (620) matching with γ-Fe_2O_3 phase. In addition, it also contains the planes (111) and (200) matching to that of the Ag present in the cubic phase (JCPDS file No. 001-1167) (Fig. 7 b''').

HR-TEM images of the SB and SPHAg exhibited lattice fringes with the d-spacing 0.295 nm (Figs. 7 a'''' and 7 b''''), which matches with the d spacing corresponding to (220) plane of γ-Fe_2O_3 phase suggesting it to be present in both the samples. In case of SPHAg, the presence of Ag could also be confirmed by the presence of lattice fringes, which corresponded to the (111) plane of silver in cubic phase (7 b'''''). From several such images of: SB, the size of γ-Fe_2O_3 NPs was found to be 11.6 ±1.6 nm; whereas, for SPHAg, the size of γ-Fe_2O_3 and Ag NPs were estimated to be 9 ± 1 and 6.6 ± 0.6 nm, respectively.

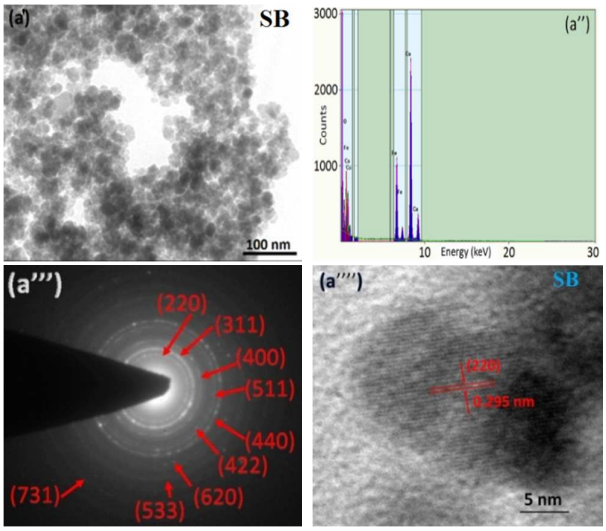

Fig. 7(A)- (a') TEM images;(a'') EDAX analysis; (a''') SAED pattern and (a'''') HR-TEM image of SB.

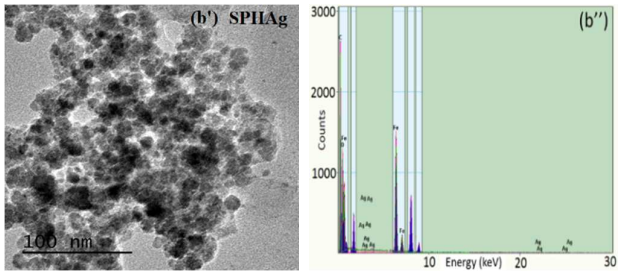

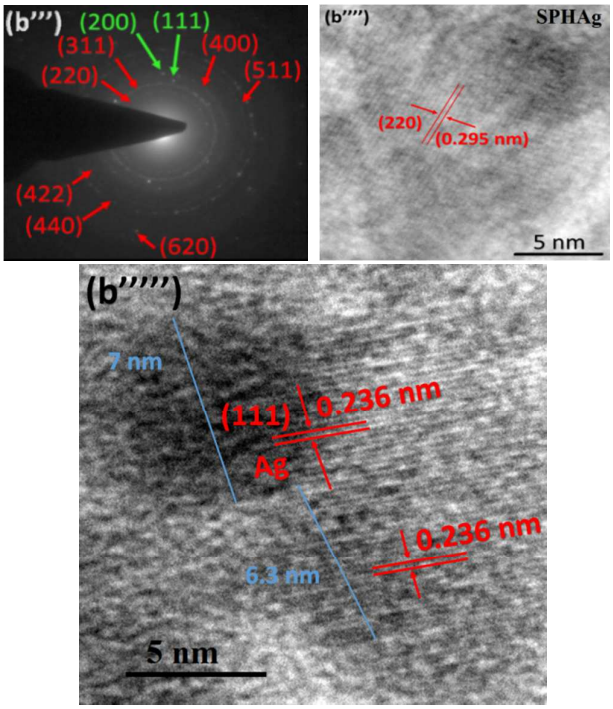

Fig. 7(B)- (b') TEM images; (b'') EDAX analysis; (b''') SAED pattern and HR-TEM image of γ-Fe_2O_3 NPs (b'''') and Ag NPs (b''''') in SPHAg.

BET

The observed decrease in the size of nanoparticles was examined by determining the BET surface area of SB, SPLAg and SPHAg, which it is found to follow the order: SB (61.721 m^2/g) < SPLAg (65.17 m^2/g) < SPHAg (75.08 m^2/g) after 2 h degassing. It suggests that the addition of Ag NPs results in an increase in the surface area indicating the size of these particles to reduce as is also evidenced by AFM, FESEM and TEM analyses.

Magnetic measurement

The magnetic behavior of SPLAg and SPHAg along with SB was analyzed by recording the hysteresis loops (M-H curve) at 300 K and 5 K (Fig. 8). All the samples at 300 K exhibit the superparamagnetic behavior without any appreciable coercivity and remanance and attain a saturation magnetization at field greater than 0.5 kOe. A comparison of the values of saturation of magnetization (M_s in emu/g) indicates them to increase in the order: SB (59) > SPLAg (63) > SPHAg (69). Moreover, the value of M_s for SPHAg is observed to be to be about 20 % higher to that of SB, suggesting that the addition of Ag enhances the value of Ms.

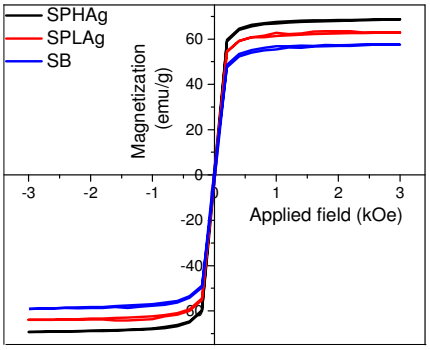

Fig. 8 M-H loop of SB, SPLAg and SPHAg at (a) 300 K.

XRD and Raman spectroscopy of the as synthesized nanocomposites reveals them to be silver coated γ-Fe_2O_3 nanocomposites containing Ag in the cubic phase (Figs. 2 and 3). XPS analysis evidently demonstrates the formation of composite consisting of γ-Fe_2O_3 and silver phase bound to glucose. A reduction in the average size of the matrix observed upon *in situ* generation of Ag NPs on γ-Fe_2O_3 matrix is understood by the breaking of weak van der Waals non-covalent interactions within γ-Fe_2O_3 clusters upon generation of Ag. This is also evidenced by the optical absorption spectrum of Ag coated γ-Fe_2O_3 nanocomposites at its low and high concentration exhibiting increasing blue shift in the absorption spectra (Fig. 1c and 1d). The surface effects observed upon increasing addition of Ag causing a reduction in the size of the Ag – γ-Fe_2O_3 nanoclusters, suggests them to bring a change in the orientation of the surface spin due to increased supramolecular interactions, resulting in an enhanced magnetization (Fig. 8).

Catalytic reduction of 4-Nip

In control experiments the feasibility of reduction of 4-Nip was examined by $NaBH_4$ alone and $NaBH_4$ on the γ-Fe_2O_3 matrix in the absence of Ag NPs (Fig. S5, ESI†). Under these conditions no reduction of 4-Nip was observed up to 180 min and virtually no change in the absorption due to 4-Nip was noted, suggesting the absence of involvement of $NaBH_4$ alone as well as $NaBH_4$ on the γ-Fe_2O_3 matrix in the reduction process. This reaction though appears to be feasible in terms of the reduction potential of 4-Nip (E_0 for 4-Nip/4-Ap = - 0.76V) and $NaBH_4$ (H_3BO_3/BH_4^- = - 1.33V) versus NHE contrary to the above observation. Obviously, this process in not permitted kinetically.

Ag mediated catalytic reduction of 4-Nip

The kinetics of the reaction was examined by changing the concentration of silver in a wide concentration range (0.15 – 28.9 μM) by maintaining the pseudo-kinetic conditions with respect to other reactants. Under all the used kinetic conditions, the 4-Nip upon reduction is converted into 4-Ap. For a typical case, in which the concentration of the silver has been kept at 1.8 μM, $NaBH_4$ (68.22 mM) and 4-Nip (161.27 μM), the reduction process is presented in Fig. 9 a. It results in the appearance of two new peaks at 231 and 302 nm and exhibiting four isosbestic points at 224, 249, 277 and 318 nm respectively.

In order to analyze the operating mechanism the effect of concentration of Ag NPs was investigated both at its lower as well as higher concentrations. At lower concentrations of Ag, the catalytic reduction followed the first-order kinetics, whereas, at higher concentration of Ag, the zero-order kinetics is obeyed. Typical kinetic traces observed at low and high concentrations of Ag have been recorded in Fig. 9 b and c, respectively.

Effect of concentration of Ag NPs

Lower concentration range. In the first set of experiments, the concentration of Ag was varied in the range of 0.15 - 1.2 μM keeping other reactants at a much higher concentration (more than ten times) so as to maintain the pseudo-kinetic conditions. In all the kinetic experiments, an induction period was noted, the duration of which is observed to reduce with an increase in the concentration of Ag.

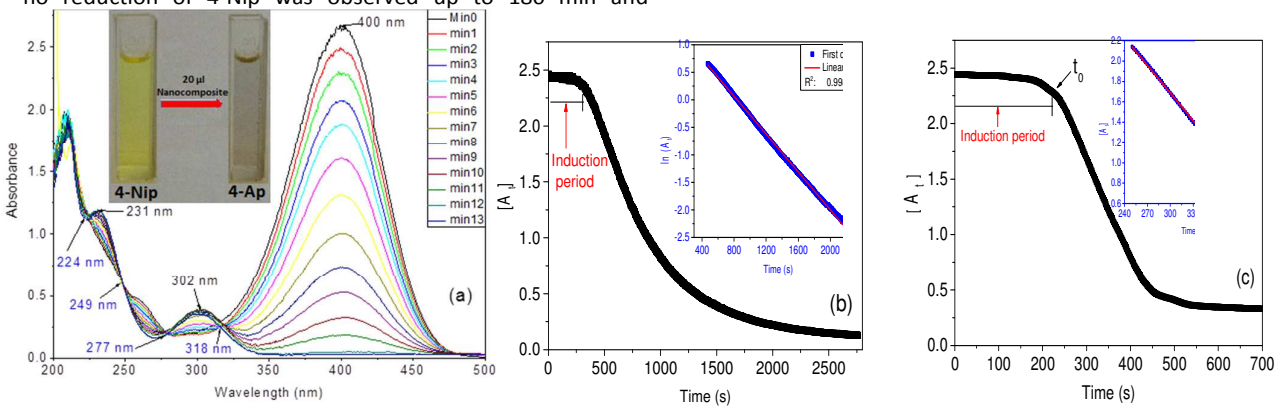

Fig. 9 (a) Absorption spectra of 4-Nip depicting its catalytic reduction to 4-Ap having [Ag] = 1.8 μM, [$NaBH_4$] = 68.22 mM, [4-Nip] = 161.27 μM. Inset: Digital image exhibiting the reduction of 4-Nip to 4-Ap. Kinetic traces depicting reduction of 4-Nip recorded at different concentrations of silver (b) 0.3 μM; (c) 3.2 μM, [$NaBH_4$] = 68.22 mM, [4-Nip] = 161.27 μM at 30^0 C.

In this concentration range, the reduction of 4-Nip following pseudo-first-order rate constant was found to vary linearly with the concentration of Ag NPs (Fig. 10 a), from which the second order rate constant was determined from the slope of the graph to be 5.28×10^3 $dm^3 mol^{-1} s^{-1}$.

The used pseudo-conditions, specifically the concentration of $NaBH_4$ and 4-Nip were examined by varying their concentrations within a small range. The kinetic plots obtained from these experiments by varying each of the individual reactant keeping all other reactants constant are shown in Fig. 10 b and c, respectively.

For $NaBH_4$, a change in the concentration from 60 - 119 mM did not show any appreciable change in rate constant, but a decrease in its concentration to 51.2 mM, however, led to a slight decrease in rate constant value (Fig 10 b). It suggests the reaction to be independent of the BH_4^- concentration.

For 4-Nip variation (64.5 - 178 µM) a change in the kinetic behavior is recorded in Fig. 10 c. Interestingly, at lower concentrations of 4-Nip (64.5 to 104 µM), the rate constant increases with an increase in [4-Nip] and was found to be the maximum at 113 µM, thereafter, it starts decreasing from 113 to 178 µM. At very low concentrations of 4-Nip the surface is largely occupied by BH_4^-, which results in relatively lower values of rate constant. A further increase in the concentration of 4-Nip the surface gets increasingly occupied by more Nip molecules, causing an increase in the rate constant. The higher concentrations of Nip, however, interferes in the reaction with BH_4^- due to higher binding constant for 4-Nip compared to that of BH_4^-, as has also been observed in other Ag catalyzed reactions,[63] resulting in a decrease in the rate constant. At a fixed concentration of other reactant this is the characteristic feature of the surface catalyzed reaction following the Langmuir-Hinshelwood model (Fig. 10 c). Since the concentration of BH_4^- in these experiments is in large excess (68.22 mM) to that of 4-Nip (113 µM), therefore, at low concentrations of Ag the observed kinetics exhibits the first-order with respect to 4-Nip and the reaction follows pseudo-first-order behavior. The observed rate constant is, therefore, considered to be the apparent first-order kinetic constant (k_{Ap}).

Higher concentration range. Since at higher concentrations of Ag (> 2.4 µM) the kinetics starts deviating from the first-order behavior, kinetic experiments at relatively higher concentrations of Ag (3.2 - 28.9 µM) were performed by keeping the concentrations of other reactants such that the pseudo-conditions are maintained. The kinetic data of these runs exhibit zero-order kinetics (Fig. 10 a').

As expected under these conditions, the reduction of 4-Nip gets over efficiently within 5 min excluding induction period.

To further examine the above kinetic behavior, the effect of concentration of all other reactants, namely, $NaBH_4$ (51.2 - 119 mM) and 4-Nip (146 - 194 µM) was varied, keeping the concentration of silver constant. The kinetic traces of these runs are shown in Fig. 10 b' and c'.

From these experiments it is evident that a slight variation from the pseudo-conditions results in the marked deviation in the rate constant associated with a mixed kinetic behavior.

Analysis of thermodynamic parameters

The thermodynamic parameters for the above studied reaction were obtained by performing the effect of temperature on the rate of reduction of 4-Nip for the typical concentrations of Ag at 0.6 µM and 6.4 µM in the lower and higher concentration range, respectively by keeping the concentrations of $NaBH_4$ (68.22 mM) and 4-Nip (113 / 161 µM) constant. These experiments were performed in the temperature range of 20 – 50^0 C. In these experiments, it was observed that the induction period decreases with an increase in temperature. The activation energy and other thermodynamic parameters ($\Delta H^{\ddagger}$, $\Delta G^{\ddagger}$ and $\Delta S^{\ddagger}$) were obtained using the thermodynamic formulations derived from the absolute reaction rate theory[64] (Fig.11 a and b).

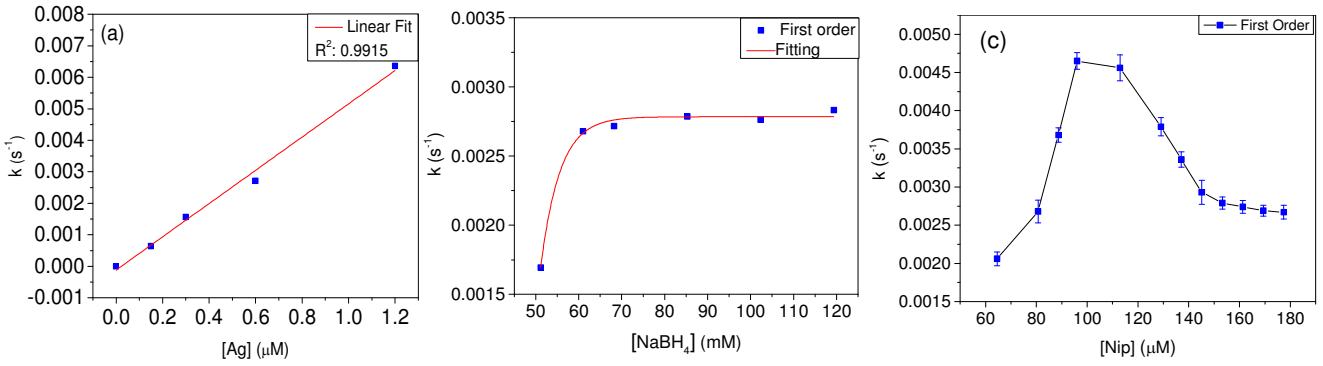

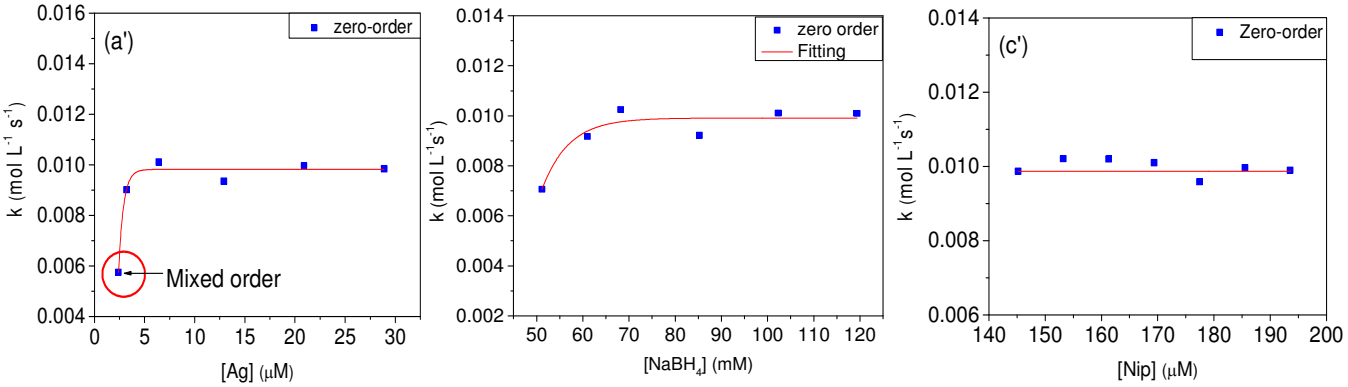

Fig. 10 Kinetic data exhibiting effect of concentrations of at 30^0 C: Silver (a) first-order rate constant (k) as a function of [Ag] = (0.15 -1.209 μM), [4-Nip] = 161.27 μM, [$NaBH_4$] = 68.22 mM; $NaBH_4$ (b) [$NaBH_4$] = (51.2 -119.3 mM) having [Ag] = 0.6 μM, [4-Nip] = 161.27 μM and 4-Nitrophenol (c) [4-Nip] = (64.5 -178 μM), [$NaBH_4$] = 68.22 mM and [Ag] = 0.6 μM. Rate constant as a function of concentration: Silver (a') [Ag] = (3.2 -28.9 μM), [4-Nip] = 161.27 μM, [$NaBH_4$] = 68.22 mM; $NaBH_4$ (b') [$NaBH_4$] = (51.2 -119.3 mM), [4-Nip] = 161.27 μM and [Ag] = 6.4 μM and 4-Nitrophenol (c') [4-Nip] = (146 -194 μM) having [$NaBH_4$] = 68.22 mM and [Ag] = 6.4 μM at 30^0 C

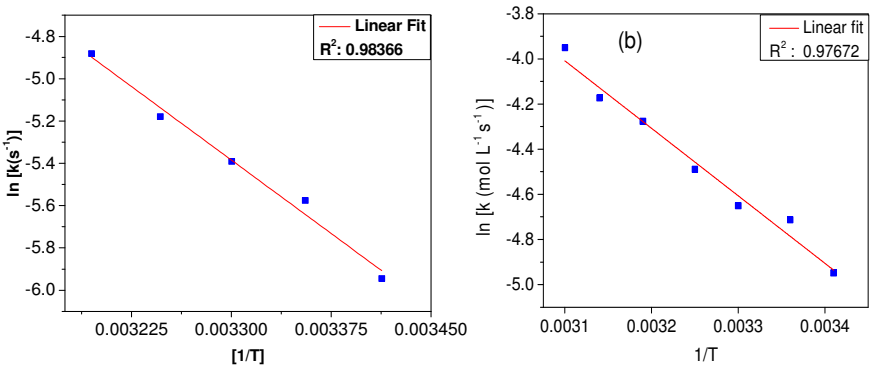

Fig. 11 Plot of ln (k) versus (1/T) for the 4-Nip reduction in the presence of Ag – γ- Fe_2O_3 nanocomposite containing [$NaBH_4$] = 68.22 mM: (a) low [Ag] = 0.6 μM and [4-Nip] = 113 μM; (b) high [Ag] = 6.4 μM and [4-Nip] = 161 μM.

Table 1 Calculated thermodynamic parameters for low and high concentration of Ag NPs.

Catalyst [Ag]	Order of reaction	E_A (kJ mol^{-1})	$\Delta G^{\ddagger}$ (kJ mol^{-1})	$\Delta H^{\ddagger}$ (kJ mol^{-1})	$\Delta S^{\ddagger}$(J $mol^{-1}K^{-1}$)
0.6 μM	first-order	38.9	87.8	36.4	- 169
6.4 μM	zero-order	25.0	86.0	22.4	- 210

Mechanism

The reduction of 4-Nip is conceived to occur by the donation of electron from BH_4^- to the acceptor 4-Nip adsorbed on the surface of the catalyst (Ag – γ-Fe_2O_3) in a bimolecular reaction. In these experiments, the surface of the particles (S) is a composite of Ag – γ-Fe_2O_3 (X) containing adsorbed BH_4^- and is denoted by S_X. Since the reaction is initiated only in the presence of Ag NPs and γ-Fe_2O_3 does not contribute to the reaction, it is likely that BH_4^- initially transfer the electrons to Ag NPs, which then reduces 4-Nip to 4-Ap (Scheme 1).

The observed change in kinetics with an alteration in concentration of Ag suggests that the sites available on the surface of the catalyst influence the kinetics in a complex scheme. Since BH_4^- is initially mixed with 4-Nip and the reaction is initiated by the addition of Ag NPs, the duration of the induction period should be controlled by the 4-Nip approaching to these sites. Indeed, the induction period reduces with increase in the concentration of Ag (0.15 - 28.9 μM) from 320 s to 61 s. Increasing sites essentially allows more molecules of 4-Nip to get adsorbed on their surface to undergo reduction. It indirectly determines the concentration of 4-Nip available for the reaction on its surface.

Since at low concentrations of Ag the reduction follows first-order kinetics and at high concentrations it follows zero-order kinetics (Table 1), from the above kinetic data this behavior is understood by the surface reactions having 4-Nip molecules adsorbed on the surface of the catalyst. The occurrence of the above reaction could be best explained in terms of Langmuir-Hinshelwood model.[64]

Scheme 1 Mechanism for the reduction of 4-Nip to 4-Ap on silver coated γ-Fe_2O_3 nanocomposites (Ag – γ-Fe_2O_3)

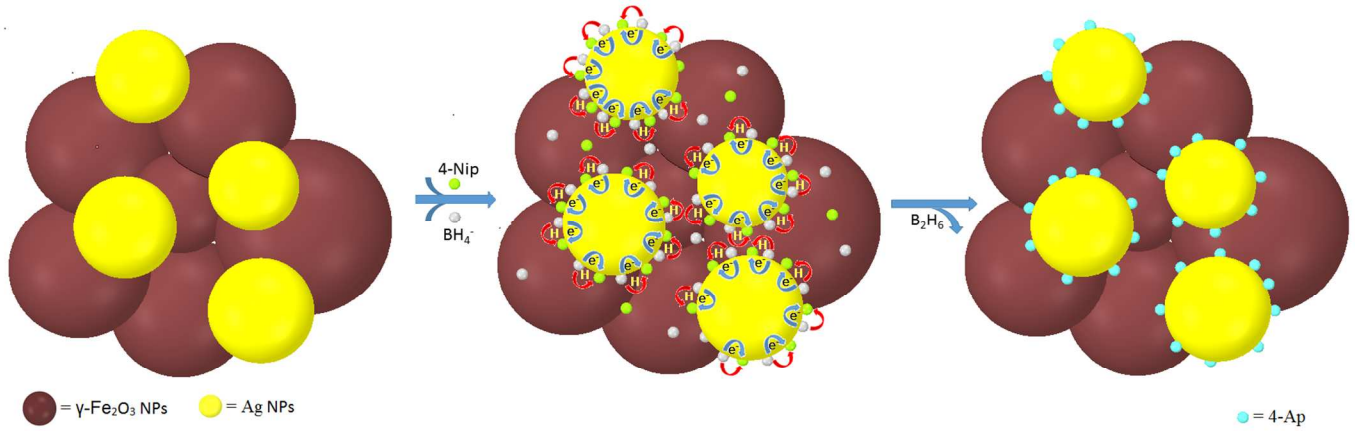

The mechanism for the occurring reaction may be presented as:

$$4\text{-}Nip + S_{(Ag\,-\,\gamma\text{-}Fe_2O_3\ NC)} \rightleftharpoons [4\text{-}Nip - S_X] \xrightarrow{slow} (4\text{-}Ap - S_X) \rightleftharpoons 4\text{-}Ap + S_X$$

The rate of reaction then will be –

$$-\frac{d[4\text{-}Nip]}{dt} = k_{Ap}\theta_X$$

where, θ_X represents the fraction of bare sites on the matrix and $[4\text{-}Nip - S_X]$ denotes the concentration of the species consisting of the 4-Nip bound to the surface site. k_{Ap} represents the apparent rate constant of the reaction.

$$-\frac{d[4\text{-}Nip]}{dt} = \frac{K_{4\text{-}Nip}[4\text{-}Nip]}{1 + \left(K_{4\text{-}Nip}[4\text{-}Nip]\right) + \left(K_{4\text{-}Ap}[4\text{-}Ap]\right)}$$

$K_{4\text{-}Nip}$ and $K_{4\text{-}Ap}$ denote the equilibrium constants between 4-Nip and the surface and 4-Ap and the surface, respectively.

Thus the rate constant from the above rate law will depend on the relative values of $(K_{4\text{-}Nip}[4\text{-}Nip])$ and $(K_{4\text{-}Ap}[4\text{-}Ap])$. At low concentration of the catalyst both 4-Nip and 4-Ap are relatively weakly adsorbed, under these conditions $\{\left(K_{4\text{-}Nip}[4\text{-}Nip]\right) + \left(K_{4\text{-}Ap}[4\text{-}Ap]\right)\}$<< 1. Therefore, the reaction follows the first-order kinetics.

On the other hand, at high concentrations of catalyst, 4-Nip is relatively more strongly adsorbed on the surface as compared to that of the product. Under such conditions $\left(K_{4\text{-}Nip}[4\text{-}Nip]\right)$ >>$\{\left(K_{4\text{-}Ap}[4\text{-}Ap]\right)+1\}$ and the reaction would then follow zero-order kinetics.

The weak binding of 4-Nip at low concentrations of silver and relatively stronger binding at its high concentration(s) in the transition state is also reflected by thermodynamic parameters in which the $\Delta S^{\ddagger}$ at lower and higher concentrations are -169 and -210 J mol^{-1} K^{-1}, respectively. These values suggest the formation of more ordered structure at higher concentrations of Ag which is also supported by the AFM, FESEM and TEM data (Figs. 5-7).

Catalytic efficiency and reusability of the nanocomposites

At low concentrations of Ag NPs, the rate constant for the reduction of 4-Nip varies linearly with the concentration of Ag NPs (Fig. 8 a) associated with a reduction in the induction period. It evidently suggests the catalytic efficiency in low Ag NPs concentration range to be quite effective for the reduction of 4-Nip. It was further verified experimentally by repetitive use of the catalyst (up to seven times) without any catalytic loss. The conversion efficiency and the time taken for complete conversion by the catalyst are presented in Fig. 12. The very similar efficiency with a marginal increase in reaction time after the reuse of the catalyst for 7 times indicates that the catalyst maintains its catalytic activity in the process of reduction. The above observations clearly demonstrate that fairly small amount of Ag NPs to be highly effective for the reduction as compared to the most of the earlier reported work.[28,41-44]

A comparison of the present nanocomposite with those somewhat related systems investigated previously[45,65] are presented in Table 2 as regards to their synthesis and characteristic features. This table clearly reveals that the as synthesized nanocomposites contains the highest value of magnetization with the minimum amount of Ag NPs and exhibits fairly high catalytic activity for the reduction of 4-Nip.

In order to assess the role of glucose as stabilizer and reducing agent, in a control experiment the *in situ* generation of Ag was also carried out by using $NaBH_4$ as reducing agent. By employing the same concentration of Ag NPs produced by using $NaBH_4$ on γ-Fe_2O_3 matrix as used in the present system, the rate constant for the catalytic reduction of 4-Nip was found to be 1.6 times smaller to that of glucose mediated nanosystems under identical experimental conditions (Fig. S7, ESI†). It suggests that besides glucose being biocompatible and non-toxic serves as a better stabilizer and reducing agent generating Ag NPs providing more catalytic sites on the surface of matrix. To the best of our knowledge this is the lowest concentration of Ag NPs employed for the 4-Nip reduction in such systems.

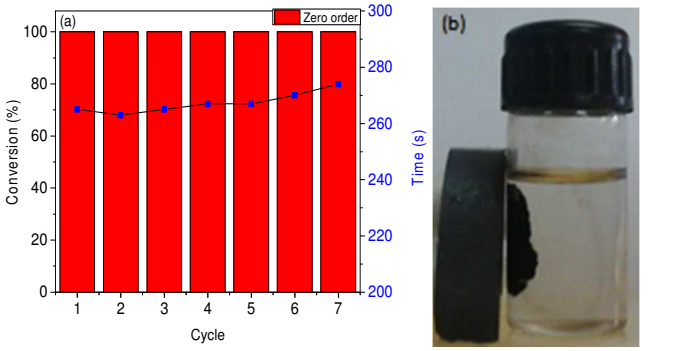

Fig. 12 (a) Graph showing the variation in the time of completion of full conversion of 4-Nip to 4-Ap for up to 7 cycles and (b) Digital image showing the easy separation of the nanocomposite and reusability of the catalyst employing external magnetic field for large scale reactions.

Table 2: Comparison of synthetic protocol and characteristic features of the as synthesized Ag – γ-Fe_2O_3 nanocomposite with similar reported nanosystems.

Catalyst used	Ag wt (%) employed	Method of preparation and phase	size	Magnetization (emu/g)	k_{app} (s^{-1}) (Temp)	Order of reaction	Mechanism/ Model	Reference s
Ag-γ-Fe_2O_3	52	γ-Fe_2O_3 (commercial) Ag deposited in ethanolic medium using butylamine as reducing agent	33 ± 19 nm (γ-Fe_2O_3) 5-10 nm (Ag)	Not reported	15 ×10^{-3} (35^0C)	First	-	45
Ag supported iron oxide microbox	2.5 - 10	Aqueous, High temp. (350° C) synthesis; mixed Phase (γ-Fe_2O_3 and α-Fe_2O_3)* containing Ag	Size of Fe_2O_3 not reported 16.8-28 nm (Ag)	~ 20 with hysteresis loop	2.33-14×10^{-3} (20^0C)	First	Mechanism proposed	65
Ag – γ-Fe_2O_3	0.05-0.43 (0.15-1.2 μM)	Aqueous, Glucose mediated in situ Ag generation; γ-Fe_2O_3 synthesized and characterized by Raman, XRD, XPS	9 ± 1 nm (γ-Fe_2O_3) 6.6 ± 0.6 nm (Ag)	63 (superpara-magnetic)	0.6-6.4× 10^{-3} (30^0C)	First	Mechanism analyzed (Langmuir-Hinshelwood kinetic model)	This work
	1.15 (3.2 μM)			69 (superpara-magnetic)	9.02 ×10^{-3} mol L^{-1} s^{-1} (30^0C)	Zero		This work

(composition not reported)*

Conclusions

We have successfully synthesized Ag – γ-Fe_2O_3 multifunctional nanocomposites consisting of both γ-Fe_2O_3 and Ag in the cubic phase in aqueous medium employing the green approach. The *in situ* coating of the Ag on the surface of γ-Fe_2O_3 matrix results in its homogeneous distribution causing a reduction in the size of the γ-Fe_2O_3 nanoclusters. The silver coated nanocomposite catalyzes the reduction of hazardous 4-Nip to useful environmental benign product, 4-Ap and exhibits the concentration dependent kinetics following the Langmuir-Hinshelwood mechanism. Glucose being environmentally benign, displaying weak non-covalent interactions with Ag and γ-Fe_2O_3 in the composite through –OH and –C=O functional groups, not only serves as an effective stabilizer but also enhances the homogeneous reactive sites in its surface, thereby, increasing the catalytic activity. The higher conversion efficiency at relatively lower concentrations of silver demonstrates this nanosystem to be of great significance as regard to their catalytic activity. The enhanced catalytic activity observed in the present work is in line with the preliminary experiments demonstrating efficient antibacterial activity. Thus, the as synthesized nanocomposites, being magnetically separable and recyclable with superparamagnetic features, having high magnetization and surface area, demonstrating efficient catalytic activity indicates it to be environmentally benign multifunctional material, promising for catalytic and biological applications.

Acknowledgements

Financial support of CSIR, New Delhi (Grant no. 01/2758/13/EMR-II) to undertake this work is gratefully acknowledged. Mandeep Kaloti is grateful to MHRD, New Delhi for the award of SRF. Thanks are also due to head IIC, IIT Roorkee for providing the facilities of FESEM, AFM, TEM and XRD.

References

1 W. Wu, Q. He and C. Jiang, *Nanoscale Res. Lett.*, 2008, **3**, 397-415.
2 T. Hyeon, *Chem. Commun.*, 2003, 927-934.
3 I. Torres-Diaz and C. Rinaldi, *Soft matter*, 2014, **10**, 8584-8602.

4 P. Quaresma, I. Osorio, G. Doria, P. A. Carvalho, A. Pereira, J. Langer, J. P. Araujo, I. Pastoriza-Santos, L. M. Liz-Marzan, R. Franco, P. V. Baptista and E. Pereira, *R, Soc. Chem. Adv.*, 2014, **4**, 3659-3667.
5 C. Sun, J. S. H. Lee and M. Zhang, *Adv. Drug Deliv. Rev.,* 2008, **60**, 1252-1265.
6 R. Hergt, S. Dutz, R. Müller and M. Zeisberger, *J. Phys.: Condens. Matter*, 2006, **18**, S2919-S2934.
7 H. Y. Cheng, L.J. Lai and F.H. Ko, *Int. J. Nanomedicine*, 2012, **7**, 2967-2973.
8 J. B. Haun, T.-J. Yoon, H. Lee and R. Weissleder, *WIREs Nanomed. Nanobiotechnol.,* 2010, **2**, 291-304.
9 R. Sensenig, Y. Sapir, C. MacDonald, S. Cohen and B. Polyak, *Nanomedicine,* 2012, **7**, 1425-1442.
10 R. Di Corato, N. C. Bigall, A. Ragusa, D. Dorfs, A. Genovese, R. Marotta, L. Manna and T. Pellegrino, *ACS Nano*, 2011, **5**, 1109-1121.
11 J. Won, M. Kim, Y. W. Yi, Y. H. Kim, N. Jung and T. K. Kim, *Science*, 2005, **309**, 121-125.
12 J. Govan, Y. K. Gun'ko and Y. ko, *Nanomaterials*, 2014, **4**, 222-241.
13 F. Y. Dai, M. Du, Y. Liu, G. Liu, Q. Liu and X. Zhang, *J. Mater. Chem. B.,* 2014, **2**, 2240-2247.
14 Y. Ge, Y. Zhang, S. He, F. Nie, G. Teng and N. Gu, *Nanoscale Res. Lett.*, 2009, **4**, 287-295.
15 X. Q. Xu, H. Shen, J. R. Xu, M. Q. Xie and X. J. Li, *Appl. Surf. Sci.*, 2006, **253**, 2158-2164.
16 D. K. Kim, M. Mikhaylova, F. H. Wang, J. Kehr, B. Bjelke, Y. Zhang, T. Tsakalakos and M. Muhammed, *Chem. Mater.,* 2003, **15**, 4343-4351.
17 W. Xiong, Y. Guan, C. Guo, M. Yang, T. Xia and S. Zhao, *J. Appl. Polym. Sci.,* 2014, **131,** 40777.
18 A. Ruiz, G. Salas, M. Calero, Y. Hernández, A. Villanueva, F. Herranz, S. Veintemillas-Verdaguer, E. Martínez, D. F. Barber and M. P. Morales, *Acta biomater.*, 2013, **9**, 6421-6430.
19 H. Y. Lee, S. H. Lee, C. Xu, J. Xie, J. H. Lee, B. Wu, A. L. Koh, X. Wang, R. Sinclair, S. X. Wang, D. G. Nishimura, S. Biswal, S. Sun, S. H. Cho and X. Chen, *Nanotechnology*, 2008, **19**, 165101.
20 .J. Guo, W. Yang, C. Wang, J. He and J. Chen, *Chem. Mater.*, 2006, **18**, 5554-5562.
21 A. Akbarzadeh, M. Samiei, S. W. Joo, M. Anzaby, Y. Hanifehpour, H. T. Nasrabadi and S. Davaran, *J. Nanobiotechnology*, 2012, **10**, 46.
22 N. Schleich, P. Sibret, P. Danhier, B. Ucakar, S. Laurent, R. N. Muller, C. Jerome, B. Gallez, V. Preat and F. Danhier, *Int. J. Pharm.* 2013, **447**, 94-101.
23 E. S. Vasquez, I. W. Chu and K. B. Walters, *Langmuir*, 2014, **30**, 6858-6866.
24 Y. Zhou, Z. Tang, C. Shi, S. Shi, Z. Qian and S. Zhou, *J. Mater. Sci. Mater. Med.*, 2012, **23**, 2697-2708.
25 F. Bao, J. L. Yao and R. A. Gu, *Langmuir*, 2009, **25**, 10782-10787.
26 P. Granitzer, K. Rumpf, Y. Tian, G. Akkaraju, J. Coffer, P. Poelt and M. Reissner, *Appl. Phys. Lett.*, 2013, **102**, 193110.
27 S. L. C. Pinho, G. A. Pereira, P. Voisin, J. Kassem, V. Bouchaud, L. Etienne, J. A. Peters, L. Carlos, S. Mornet, C. F. G. C. Geraldes, J. Rocha and M.-H. Delville, *ACS Nano*, 2010, **4**, 5339-5349.
28 Y. Chi, Q. Yuan, Y. Li, J. Tu, L. Zhao, N. Li and X. Li, *J. Colloid Interface Sci.,* 2012, **383**, 96-102.
29 Y. Zhang, B. Chen, L. Zhang, J. Huang, F. Chen, Z. Yang, J. Yao and Z. Zhang, *Nanoscale*, 2011, **3**, 1446-1450.
30 M. Li and G. Chen, *Nanoscale*, 2013, **5**, 11919-11927.
31 J. Tang, L. Feng and J. A. Wiemann, *Appl. Phys. Lett.*, 1999, **74**, 2522-2524.
32 D. H. Zhang, G.-D. Li, J. X. Li and J. S. Chen, *Chem. Commun.*, 2008, 3414-3416.
33 S. Wunder, F. Polzer, Y. Lu, Y. Mei and M. Ballauff, *J. Phys. Chem. C*, 2010, **114**, 8814-8820.
34 B. Chudasama, A. Vala, N. Andhariya, R. V. Upadhyay and R. V. Mehta, *Nano Res.*, 2009, **2**, 955-965.
35 J. Chen, Z. Guo, H. B. Wang, M. Gong, X. K. Kong, P. Xia and Q. W. Chen, *Biomaterials*, 2013, **34**, 571-581.
36 J. A. Johnson, J. J. Makis, K. A. Marvin, S. E. Rodenbusch and K. J. Stevenson, *J. Phys. Chem. C*, 2013, **117**, 22644-22651.
37 N. C. Antonels and R. Meijboom, *Langmuir*, 2013, **29**, 13433-13442.
38 J. Zheng, Y. Dong, W. Wang, Y. Ma, J. Hu, X. Chen and X.Chen, *Nanoscale,* 2013**, 5**, 11, 4894-4901.
39 S. Saha, A. Pal, S. Kundu, S. Basu and T. Pal, *Langmuir*, 2009, **26**, 2885-2893.
40 S. K. Das, M. M. R. Khan, A. K. Guhab and N. Naska, *Green Chem.*, 2013, **15**, 2548-2557.
41 B. Duan, F. Liu, M. He and L. Zhang, *Green Chem.*, 2014, **16**, 2835-2845.
42 M. K .Joshi, H. R. Pant, H. J. Kim, J. H. Kim and C. S. Kim, *Colloids Surf. A*, 2014, **446**, 102-108.
43 X. Du, J. He, J. Zhu, L. Sun, and S. An, *Appl. Surf. Sci.*, 2012, **258**, 7, 2717-2723.
44 J. R. Chiou, B. H. Lai, K. C. Hsu and D. H. Chen, *J. Hazard. Mater.*, 2013, **248–249**, 394-400.
45 K .Shin, J. Y. Choi, C. Park, H. Jang, and K. Kim, *Catal. Lett.,* 2009, **133**, 1-7.
46 S. Campelj, D. Makovec and M. Drofenik*, J. Phys.: Condens. Matter*, 2008, **20**, 204101.
47 R. M.Cornell and U. Schwertmann, Characterization- In The Iron Oxides; Wiley-VCH Verlag GmbH & Co. KGaA, 2004, 139-183.
48 R. A. Nyquist and R. O. Kagel, Infrared spectra of inorganic compounds. Academic press- London, 1971, 274-277.
49 N. S. Chaudhari, S. S. Warule, S. Muduli, B. B. Kale, S. Jouen, B. Lefez, B. Hannoyer and S. B. Ogale, *Dalton Trans.,* 2011, **40,** 31, 8003-8011.
50 X. Zhang, Y. Niu, X. Meng, Y. Li and J. Zhao, *CrystEngComm,* 2013, **15** ,40, 8166-8172.
51 J. Du, J. Cui and C. Jing, *Chem. Commun*, 2014, **50**, 347-349.
52 Y. Sohn, D. Pradhan, J. S. Kang and K. T. Leung, *R. Soc. Chem. Adv.*, 2015, **5**, 31472-31478.
53 G. Martínez, A. Malumbres, R. Mallada, J. L. Hueso, S. Irusta, O. Bomatí-Miguel and J. Santamaría, *Nanotechnology*, 2012, **23**, 425605.
54 J. Wang, X. Wang, Y. Song, J. Wang, C. Zhang, C. Chang, J. Yan, L. Qiu, M. Wu and Z. Guo, *Chem. Sci.*, 2013, **4**, 2605-2612.
55 T. Yamashita and P. Hayes, *Appl. Surf. Sci*, 2008, **254**, 2441-2449.
56 H. J. Li, A. Q. Zhang, Y. Hu, L. Sui, D. J. Qian and M. Chen, *Nanoscale Res. Lett*., 2012, **7**, 612.
57 S. W. Chook, C. H. Chia, S. Zakaria, M. K. Ayob, K. L. Chee, N. M. Huang, H. M. Neoh, H. N. Lim, R. Jamal and R. Rahman, *Nanoscale Res. Lett*., 2012, **7**, 541.
58 S. Dahle, J. Meuthen, W. Viöl and W. Maus-Friedrichs, *Appl. Surf. Sci*, 2013, **284**, 514-522.
59 T. Tubchareon, S. Soisuwan, S. Ratanathammaphan and P. Praserthdam, *Adv. Mater. Sci. and Engg.*, 2014, **7**, 602504.
60 G. K. Pradhan, K. H. Reddy and K. M. Parida, *Catal. Today*, 2014, **224**, 171-179.
61 C. Pereira, A. M. Pereira, P. Quaresma, P. B. Tavares, E. Pereira, Joao P. Ara□ ujo´ and C. Freire, Dalton Trans., 2010, **39**, 2842–2854.

62 S. Reiche, R. Blume, X. C. Zhao, D. Su, E. Kunkes, M. Behrens and R. Schlögl, Carbon, 2014, **77**, 175-183.
63 N. Bingwa and R. Meijboom, *J. Mol. Catal. A: Chem,* 2015, **396**, 1-7.
64 J. K. Laider, Chemical Kinetics; Pearson Education Company. 3rd Edition, 2004, 114-116.
65 Z. Jiang, D. Jiang, A. M. Showkot Hossain, K. Qian and J. Xie, *PhysChemChemPhys*, 2015, **17**, 2550-2559.

Table of Contents Graphic

Synthesis of glucose-mediated Ag - γ-Fe_2O_3 multifunctional nanocomposites in aqueous medium - a kinetic analysis of their catalytic activity for 4-nitrophenol reduction

Mandeep Kaloti,[a,b] *Anil Kumar* [a,b*] *and Naveen K. Navani* [a,c]

[a] Centre of Nanotechnology, Indian Institute of Technology Roorkee, Roorkee-247667,India
[b] Department of Chemistry, Indian Institute of Technology Roorkee, Roorkee-247667, India. *E-mail*:* anilkfcy@iitr.ac.in
[c] Department of Biotechnology, Indian Institute of Technology Roorkee, Roorkee-247667, India

Synthesis of glucose-mediated Ag - γ-Fe_2O_3 nanocomposites in aqueous medium exhibits catalytic activity for 4-nitrophenol reduction to 4-aminophenol following Langmuir-Hinshelwood mechanism at lower [Ag] (μM) (0.3, SPLAg; 6.4, SPHAg).